ENGINEERING

Autonomous microfluidic actuators for periodic sequential flow generation

Zhenglin Li and Sung-Jin Kim*

Control of periodic sequential flows of multisolutions is invaluable in a variety of technology and science applications, but it requires complex and expensive external controllers. Here, we present microfluidic systems that autonomously regulate periodic sequential flows without any user instructions or dynamic external controllers. The systems consist of astable and monostable actuators that mimic the functions of analog electronic circuits. With a constant water head pressure of the input solution acting as the sole driving force, these systems generate periodic sequential flows in a predetermined and sophisticated manner. We validate our technology with the applications that have been previously addressed only by dynamic external controllers: dynamic staining of cell nuclei and playing a touchscreen piano. Our approach provides a useful and effective alternative to dynamic external controllers.

INTRODUCTION

Control of sequential periodic flows in microfluidic chips has numerous applications, such as layer-by-layer assembly (*1*, *2*), sequential-injection analysis (*3*, *4*), soft robot actuation (*5*–*7*), and spatiotemporal analysis of cells (*8*–*12*) and organisms (*13*–*15*). These applications, however, have been mainly implemented by dynamic off-chip controllers that require many external connections and instructions for users. However, if microfluidic chips could operate in a predetermined and sophisticated manner without external instructions of the dynamic controllers, then the operation of the chips would be considerably simplified and the cost of using the dynamic controllers would be substantially reduced.

Recent microfluidic chips mimicking the operation of electronic circuits aim to implement sequential periodic multiflows without external instructions but partially achieve these functions. Microfluidic logic circuits can control sequential periodic flows, but their operation is still instructed by computer-programmed off-chip controllers (*16*–*23*). In our previous studies, we implemented fluidic switching without external controllers, but the switching was limited to only two solution flows (*24*–*26*). Recently, a fluidic timer circuit presented a six-step sequential flow, but its initiation was manually triggered without periodic operation (*27*). Therefore, a different approach that can truly implement sequential periodic flows is strongly required for the practical applications without any user instructions and external dynamic controllers.

In this work, we present a microfluidic device that produces various predetermined forms of sequential periodic flows of multiple solutions without using any dynamic controllers. The device consists of an astable actuator (AA) and a monostable actuator (MA) (Fig. 1A). The AA autonomously converts the constant pressure of two input solutions to two pulsatile out-of-phase outflows, and the MA changes the constant pressure of the input solution to a one-shot outflow by a triggered pulse pressure. The connection of the AA and MA produces a system where the MA is periodically triggered by one of the outflows of the AA. As a result, by connecting the AA with multiple MAs in parallel, various flows of multiple solutions can be implemented only with constant input pressures, thereby eliminating dynamic external controllers and user instructions (Fig. 1, B and C). These devices have control scalability for complex and sophisticated flows of multiple solutions. We demonstrate the utility of the platform by performing microfluidic operations including dynamic staining of cell nuclei with a four-step fluorescent gradient and playing a touchscreen piano with five metal rods.

Department of Mechanical Engineering, Konkuk University, Seoul 05029, Republic of Korea.
*Corresponding author. Email: yahokim@konkuk.ac.kr

RESULTS

Working principle of AA and MA systems

Figure 2A illustrates a system consisting of an AA and MA connected in parallel. The system consists of top, bottom, and elastic membrane middle layers. The channels in the top and bottom layers are filled with gray and yellow colors. The middle layer is colored with purple. Right panels of Fig. 2A depict the cross sections of the valve (section JJ′) and elastic membrane capacitor (section KK′) of MA at the moment when the valve is open. In Fig. 2B (Fig. 2C), red and blue arrows (green arrows) show the outflow paths at the top layer of the AA (MA), respectively. Black arrows depict the flows of control solutions, which regulate the opening and closing of the AA and MA valves. The pressure at the valve outlet (P_{Vo}), pressure at the valve bottom side (P_{Vb}), and pressure at the membrane capacitor topside (P_{Ct}) are the variable pressures of the MA (Fig. 2A). In the AA, the top side of the right-sided membrane capacitor has the same pressure as P_{Ct}. In turn, the constant pressures of the MA are the pressure at the inlet (P_i), pressure at the outlet (P_o), and reference pressure (P_{ref}); the constant pressures of the AA are the pressures at reference (P_{Aref}), inlet (P_{Ai}), and outlet (P_{Ao}). These constant pressures are obtained from the water head pressure of the reservoirs and are $P_i = P_{Ai} = 5$ kPa, $P_o = P_{Ao} = -5$ kPa, $P_{ref} = 7$ kPa, and $P_{Aref} = 0$ kPa.

The operational process of the system is explained with the pressure change in the AA and MA. The AA shown in Fig. 2A has two elastic membrane capacitors (M_L and M_R) and two valves (V_L and V_R). The subscripts L and R denote the left and right sides of the AA, respectively. Owing to the height difference among the reservoirs, the pressure condition is $P_{Ai} > P_{Aref} > P_{Ao}$. The AA has two states (Fig. 2C): V_R is open (state *a*1) and closed (state *a*2). The opening of V_R abruptly increases the pressures on the bottom and top sides of M_R, whereas the closing of V_R suddenly decreases those of M_R, owing to the high P_{Ai} and low P_{Ao}. When V_R opens, V_L closes (state *a*1 in Fig. 2B). This is because the opening of V_R rapidly increases the pressure on the bottom side of M_R, and this pressure closes V_L through the motion of control liquid (black arrow). Afterward, the high pressure at the bottom side of V_L is gradually decreased through the channel connected to the reference

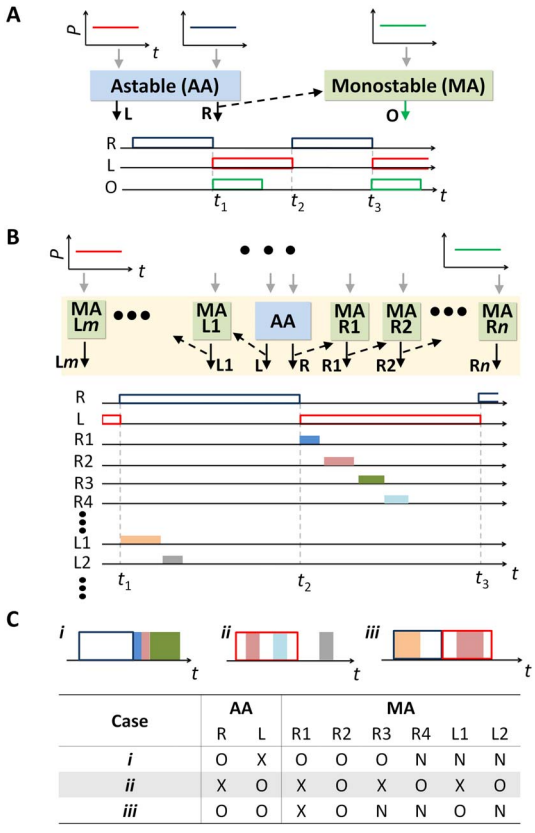

Case	AA		MA					
	R	L	R1	R2	R3	R4	L1	L2
i	O	X	O	O	O	N	N	N
ii	X	O	X	O	X	O	X	O
iii	O	O	X	O	N	N	O	N

Fig. 1. Schematic of AA and MA. (**A**) Diagram of AA and MA connected in parallel. AA autonomously converts the constant pressure (*P*) of two input solutions in its two input channels (gray arrows) to two pulsatile out-of-phase outflows in its two output channels (L and R, black arrows). Through a trigger channel (black dashed arrow) that connects R and MA, AA triggers MA only at the moment when the flow in R stops (times t_1 and t_3). Simultaneously, MA produces one-shot outflow in its output channel (O, green arrow). A solution applied to an input channel moves to its corresponding output channel without meeting with other solutions. The outflow of L does not trigger MA. (**B**) Flows in each output channel of the system with AA and multiple MAs. The top panel shows that MAs are on the right side (MA R1 to MA R*n*) and the left side (MA L1 to MA L*m*) of AA. In the bottom panel, square pulses in each time axis denote flow timing of an input solution in the corresponding output channel, and the color of the pulse corresponds to input solution. Flow in R1 (L1) is triggered by the flow termination in R (L). Similarly, flow in R2 (L2) is triggered by the flow termination in R1 (L1). In this way, sequential triggering occurs. This cycle is repeated by AA. (**C**) Generation of various flows at a target channel (T). T is connected to the output channels of MAs and AA. In the cases *i* to *iii*, the flows in T are generated by different connection combinations between T and the output channels. The symbol (O) denotes the connection between T and the corresponding output channels, the symbol (X) denotes the disconnection between them, and the symbol (N) denotes no use of the corresponding output channel and MA.

port with P_{Aref}. Then, V_L opens and V_R closes (state *a*2 in Fig. 2B). In this manner, the opened and closed states of V_L and V_R alternate, generating pulsatile pressure at the trigger channel to influence the MA (Fig. 2B). In state *a*1 (*a*2), P_{Ct} that is the pressure on the top side of M_R is high at 5 kPa (low at −5 kPa) (Fig. 2D, top). The detailed working process of the AA is explained in our previous study (*24*, *25*).

MA has three states (Fig. 2C): The MA valve is closed (state *b*1), open (state *b*2), and closed (state *b*3). Note that the change in P_{Ct} influences P_{Vb}, thereby varying the states of the MA. The MA valve (Fig. 2A) is normally closed because the condition of $P_{ref} > P_i$ pushes up the membrane bottom of the MA valve. In state *b*1, the rapid rise of P_{Ct} to 5 kPa at 1 s (Fig. 2D, top) abruptly increases P_{Vb} of the MA (Fig. 2D, middle). Such a high P_{Vb} does not change the closed state of the MA valve because a high P_{Vb} only pushes the membrane bottom side of the MA valve. In state *b*2, the MA valve opens because the abrupt decrease of P_{Ct} to −5 kPa at 20 s (Fig. 2D, top) substantially decreases P_{Vb} (Fig. 2D, middle) and pulls down the membrane of the MA valve through the control fluid. At this time, the outflow is generated and P_{Vo} rapidly increases (Fig. 2D, bottom). Then, by the motion of the control fluid (Fig. 2C, black arrow of state *b*2), P_{Vb} gradually increases (Fig. 2D, middle). State *b*3 is initiated when the MA valve is closed at 25 s by the sufficiently high P_{Vb}. In state *b*3, if an additional MA is connected at the right side of the MA valve outlet, then the closing of the MA valve triggers the motion of the outflow (Fig. 2C, green arrow of state *b*3) and opens the additional MA valve. Consequently, if the AA and multiple MAs are connected in parallel, then they can generate periodic sequential pulse flows triggered by the AA.

To characterize the operational range of MAs connected in parallel, we derived an equation that shows the outflow duration time $[T_d^{(k)}]$ of the k^{th} MA (fig. S1)

$$T_d^{(k)} = C^{(k)} R_d^{(k)} \ln\left(\frac{P_o^{(k-1)} - P_i^{(k-1)} - P_{ref}^{(k)} + P_{Vb}^{(k)}(t_i^-)}{P_i^{(k)} - P_{cth}^{(k)} - P_{ref}^{(k)}}\right) \quad (1)$$

where the variables with superscript k ($k = 1$ to N) are the parameters of the k^{th} MA, $C^{(k)}$ is the mechanical capacitance, and $R_d^{(k)}$ is fluidic resistance of duration channels. $P_i^{(0)}$ and $P_o^{(0)}$ are the inlet and outlet pressures of the AA, respectively, and $P_{cth}^{(k)}$ is the closing threshold pressure of the valve of the k^{th} MA. t_i^- is the time just before the opening of the k^{th} MA valve. To explain the operational range of the k^{th} MA, we correspond $T_d^{(k-1)}$ to the duration of state *a*1 and $T_d^{(k)}$ to that of state *b*2. In this case, $P_{Vb}^{(k)}$ and $P_{ref}^{(k)}$ correspond to P_{Vb} and P_{ref}, respectively. Equation 1 shows that $T_d^{(k)}$ linearly depends on $R_d^{(k)}$. Figure 2E shows the experimental verification of linear dependence $T_d^{(k)} \propto R_d^{(k)}$ in the range of 2.6 s to 1 hour. As high $R_d^{(k)}$ slows down the motion of the control solution (Fig. 2C, black arrow of state *b*2), the charging time of $P_{Vb}^{(k)}$ increases accordingly (Fig. 2D, state *b*2), thereby increasing $T_d^{(k)}$. In addition, the inset of Fig. 2E shows that increasing the value of $P_{ref}^{(k)} - P_i^{(k)}$ decreases $T_d^{(k)}$. This happens because a relatively high $P_{ref}^{(k)}$ charges $P_{Vb}^{(k)}$ faster through the motion of the control flow (Fig. 2C, state *b*2) and closes the valve of the k^{th} MA earlier. As a result, it causes the reduction of $T_d^{(k)}$. In addition, we measured the operational range of the MA using the value of $T_d^{(k)}/T_d^{(k-1)}$ (fig. S2). Figure 2F summarizes the result. When $R_d^{(k)}$ is fixed and $T_d^{(k)}/T_d^{(k-1)} < \alpha$ [$\alpha = 0.7$ to 1.4 for $T_d^{(k-1)} = 5$ to 2100 s], $T_d^{(k)}$ maintains a constant value and is not affected by $T_d^{(k-1)}$. In contrast, when $T_d^{(k)}/T_d^{(k-1)} > \alpha$, pressure pulse is not generated at the k^{th} MA (Fig. 2F, gray region). For relatively short $T_d^{(k-1)}$, $P_{Vb}^{(k)}$ does not sufficiently decrease to $P_{ref}^{(k)}$ (Fig. 2D, state *b*1), then $P_{Vb}^{(k)}$ at the beginning of state *b*2 does not become sufficiently low to open the k^{th} MA valve. Consequently, the k^{th} MA valve does not open.

Periodic sequential solution switching

We present two examples of predetermined sequential periodic flows with the combinations of actuator arrays and input solutions. The first example is a periodic stepwise concentration variation of fluorescent solutions. The system consisting of one AA and six MAs (Fig. 3A

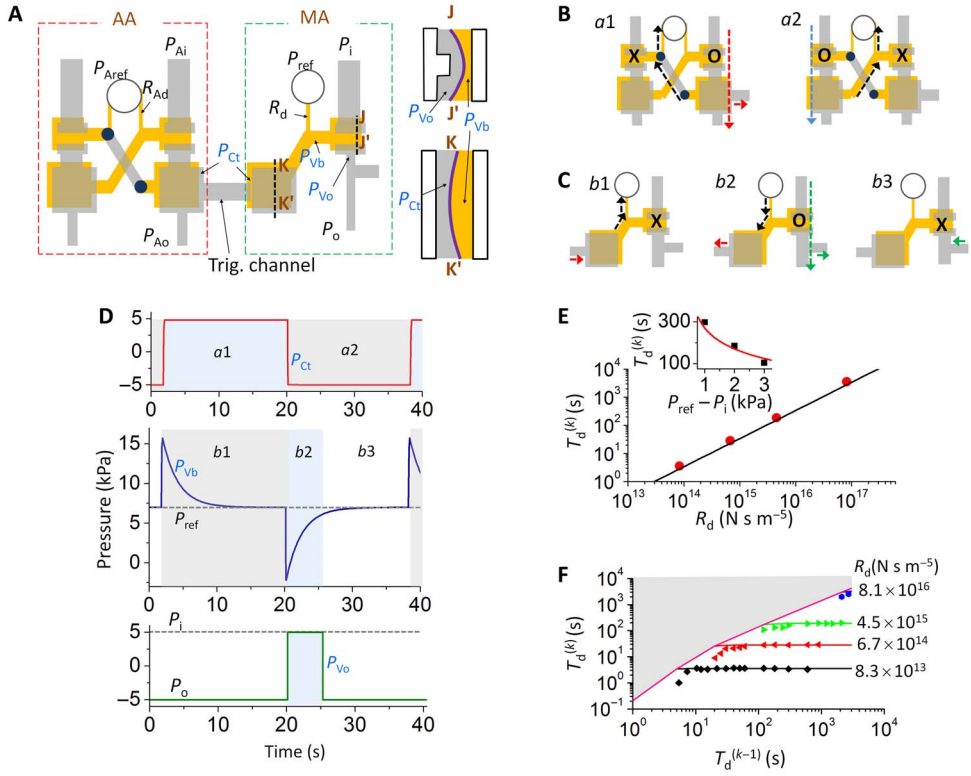

Fig. 2. Sequential and periodic switching mechanism of AA and MA. (**A**) Schematic of AA and MA. The system consists of three layers. The channels in top and bottom layers are filled with gray and yellow colors, respectively, and membrane middle layer (sections JJ′ and KK′) is colored with purple. The top and bottom layers are connected by holes (dark blue). The input, output, and reference pressures of AA (MA) are P_{Ai}, P_{Ao}, and P_{Aref} (P_i, P_o, and P_{ref}), respectively. Duration resistors of AA and MA are R_{Ad} and R_d, respectively. The top pressure of the membrane capacitors is P_{Ct}. The bottom and outlet pressures of MA valve are P_{Vb} and P_{Vo}, respectively. (**B**) Working process of AA. States *a*1 and *a*2 are defined by the open (○) and closed (×) states of the AA valves and the direction of liquid motions (arrows). (**C**) Working process of MA. States *b*1, *b*2, and *b*3 are defined by the states of MA valves and the direction of liquid motions. (**D**) Theoretical pressure profiles of P_{Ct}, P_{Vb}, and P_{Vo}. The middle panel of (D) is obtained by eq. S3. The abrupt changes of P_{Vb} at 1 and 20 s occur by the pressure continuity condition across the membrane capacitor of the MA (see eq. S7). (**E**) Pulse duration [$T_d^{(k)}$] of the k^{th} MA by R_d (points, experimental data; lines, theoretical predictions). The inset shows the control of $T_d^{(k)}$ by $P_{ref} - P_i$. (**F**) Operational ranges of $T_d^{(k-1)}$ and $T_d^{(k)}$ (points, experimental data; lines, theoretical predictions). The critical line is obtained from Eq. 1 and divides operation (white) and no-operation (gray) regions.

and fig. S3) had seven input channels (numbers 0 to 6) and one target (T) and one waste (W) output channel. Figure 3B illustrates the flow timing of the flows in each output channel of the AA (R and L), MAs (R1 to R6), and T. Figure 3C shows six states (states *a* to *f*) with different fluorescent intensities at T. When we applied the fluorescent solutions with low to high concentrations (80 to 400 μM) to input channels 1 to 5, respectively, and a blank solution to input channel 6, we could obtain states *a* to *f* (Fig. 3D, left) in a sequential and periodic manner. Using different pairings between the input channels and solutions, we could also obtain other sequential periodic profiles of fluorescent intensities (Fig. 3D, middle and right). State *f* remained for 41 s: In the target output channel, the blank solution washed the fluorescent solution for 22 s through the open valve of MA R6, and then the fluidic motion halted for 19 s in the closed valve of MA R6. The duration of state *f* for MA R6 was 41 s because the trigger interval of the AA was 66 s, whereas the outflow duration of the five MAs (MA R1 to MA R5) was 25 s.

The other example is the flow of three solutions that have different periods with overlapped intervals (Fig. 4A and fig. S4). To implement this process, we connected in parallel four MAs (MA R1 to MA R4) on the right side of the AA and two MAs (MA L1 and MA L2) on the left side of the AA. The system had three common inputs (numbers 1 to 3) and one target (T) and one waste (W) output with the connections to microfluidic channels (depicted with lines). Each actuator has its own output channel (R and L, R1 to R4, and L1 and L2). A herringbone pattern microfluidic mixer (*28*) was in the target output channel (Fig. 4A, inset); hence, in the case of two solutions flowing in parallel, the mixing occurs. Figure 4B illustrates the flow timing in each output channel. Each square pulse denotes the flow timing of each outflow in the corresponding output channel, and the color of the pulse corresponds to input solution. On the basis of the outflows of the input solution in the target channel, the target channel has eight states (states *a* to *h*). In states *a* to *d*, while the left-sided valve of AA was open, MA R1 to MA R4 were sequentially activated. As a result, the flow in T had continuous flow from L with intermittent flow from R2 and R4. In state *e*, the AA valve was still open, whereas the valves MA R1 to MA R4 were all closed because the opening time of the left-side valve of AA was longer than the total opening time of the valves MA R1 to MA R4. Thus, only the flow from L continued in T. In states *f* to *h*, the right-side valve of AA was open, and a similar process with the states *a* to *e* occurred at MA L1 and MA L2. Thus, the flow in T has a continuous flow from R with intermittent flow from L2. We applied the inputs with fluorescent solutions of blue (BF), red (RF), green (GF), and the blank solution (BS). We paired the solutions and input channels (Fig. 4B) as BF-1, RF-2, and BS-3 in Fig. 4C and GF-1, RF-2, and BS-3 in Fig. 4D. The left panels of Fig. 4 (C and D) show the corresponding outflows at the target channel, and the fluorescent intensity of each solution was

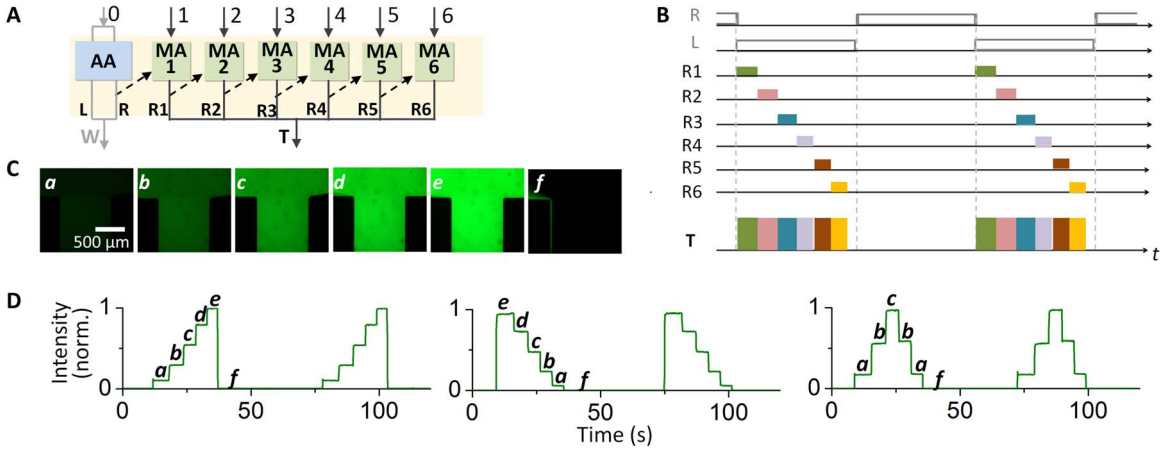

Fig. 3. Periodic variation of the concentration of output solution. (**A**) Schematic of the device consisting of one AA and six MAs (MA R1 to MA R6). The device has seven input channels (0 to 6) and one target (T) and one waste (W) output channel. Each actuator has its own output channel: R and L for AA and R1 to R6 for MA R1 to MA R6, respectively. (**B**) Flows in each output channel. Each square pulse denotes flow timing of each outflow in the corresponding output channel. (**C**) Photographs showing different fluorescent intensities (states *a* to *f*) at T output channel. (**D**) Time dependence of fluorescent intensity at T output channel determined by the concentration of fluorescent solution. For the pairs of the solution concentrations and input channels, see fig. S3.

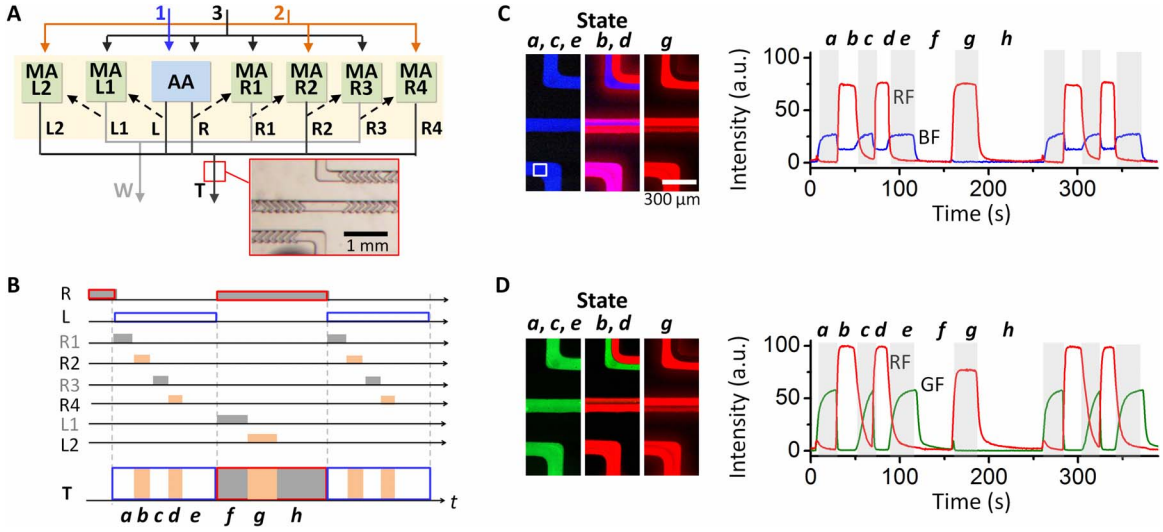

Fig. 4. Sequential and periodic variation of fluorescent intensity. (**A**) Schematic of the device having three inputs (1 to 3) and waste (W) and target (T) output channels. Each actuator has its own output channel (R and L, R1 to R4, and L1 and L2). The inset shows a micromixer in the T output channel. (**B**) Flow timing of each outflow in the corresponding output channel. On the basis of the outflows of the input solution in the target channel, the target channel has states *a* to *h*. (**C** and **D**) Periodic flow of three solutions with overlapped intervals. Fluorescent solutions of blue (BF), red (RF), green (GF), and blank solution (BS) are used. a.u., arbitrary units. For the input channels with the numbers of 1, 2, and 3 in (A), BF, RF, and BS are applied in (C), respectively, and GF, RF, and BS are applied in (D), respectively. Intensities of BF, RF, and GF are marked with blue, red, and green lines, respectively.

measured at the outlet region (Fig. 4C, white box). As shown in the right panel of Fig. 4C, the BF fluorescent intensity of states *b* and *d* was half compared to that of states *a*, *c*, and *e*. This is because, in states *b* and *d*, RF moved together with BF with the same flow rate and diluted BF, whereas in states *a*, *c*, and *e*, BF moved alone. In the right panel of Fig. 4D, the GF fluorescence of states *b* and *d* were not observed even with the simultaneous flow with GF and RF. This result is due to fluorescence resonance energy transfer (FRET) (*29*). As the wavelength bands of GF emission and RF excitation substantially overlap and their concentrations were relatively high (400 μM), GF emission was used to excite RF (fig. S5). Hence, the fluorescence of GF was extinct, whereas that of RF increased, owing to the energy transfer. The increase in RF intensity is verified by comparing states *b* and *d* with state *g* (Fig. 4D). In state *g*, RF and BS moved together, so FRET did not occur.

Dynamic staining of cell nuclei

Next, we show the system that dynamically stains cell nuclei with four steps and generates a time-varying fluorescent gradient in the nuclei. In the system (Fig. 5A and fig. S6), we arranged the AA at the top and two valves (V1 and V2) and two MAs (MA L1 and MA R1) at the bottom. The bottom of the system had four inlets for the fluorescent solution (FS) and blank solution (BS), as well as one common target output channel (T) that is connected from output channels (L1, R1, O1, and O2) of the two MAs and two valves. The flow halting in the left-side

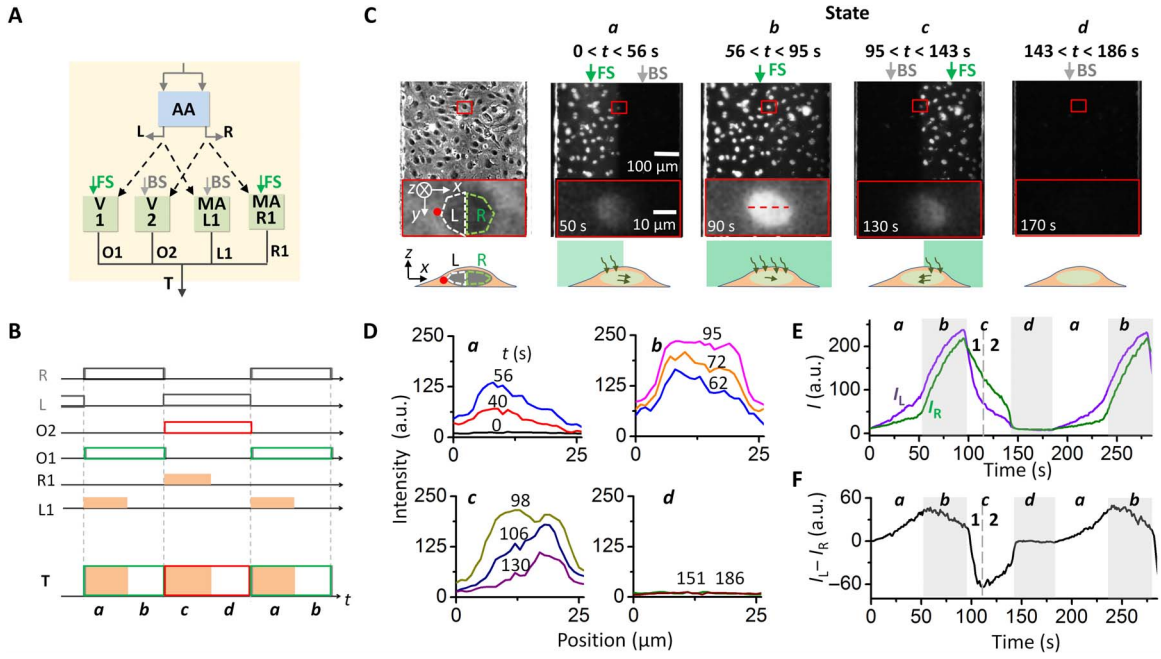

Fig. 5. Dynamic staining of cell nuclei by four-step solution switching. (**A**) Schematic of the device consisting of AA, two MAs (MA L1 and MA R1), and two valves (V1 and V2). Fluorescent (FS) and blank (BS) solutions are applied to MAs and valves and move to the target output channel (T). Each actuator has its own output channel (R and L and L1 and R1), and V1 and V2 have also output channels (O1 and O2). (**B**) Flows in each output channel. The flow in a target channel makes four states (states *a* to *d*). (**C**) Photographs showing the fluorescence variation of the nuclei of cells. The first left panel shows a phase micrograph. The bottom panels depict the diffusion process of the dye in the cell nucleus, and the diffusion direction is marked with arrows. (**D**) Intensity profile measured along the red dashed line [third panel of (C)] in states *a* to *d*. (**E**) Variation of fluorescent intensity (*I*) measured in the left (L) and right (R) regions of the cell nucleus marked with red boxes in (C). (**F**) Intensity difference ($I_L - I_R$) between L and R.

output channel (L) of the AA activated V1 and MA L1, and the flow halting in the right-side output channel (R) of the AA activated V2 and MA R1. Figure 5B illustrates how the four states (states *a* to *d*) at T are repeated. In states *a* and *b*, flow halting in L simultaneously triggers the flow in O1 and L1, resulting in two parallel flows in T (state *a*). Then, only the flow from O2 is continued in T because the valve of MA R1 closes after its pulse period while V1 remains open (state *b*). In states *c* and *d*, flow halting in R results in the flow in O2 and R1 that is similar to the process of states *a* and *b*.

Figure 5C shows cells in T that were dynamically stained during states *a* to *d* (see also movie S1). The fluorescent dye permeated the cell membranes, and fluorescent signal occurred when the dye bound with nucleic acids. Notably, the periodic switching of the blank and fluorescent solutions in T generated the variation of fluorescent intensity gradient in a cell nucleus, which was at the interface of two parallel streams (Fig. 5C, red box). The bottom panels of Fig. 5C illustrate the diffusion process of the dye in the cell nucleus, and the diffusion direction is marked with arrows. The red dot in the first panel denotes the position of the *x*-*y*-*z* coordinate. We measured the fluorescent intensity profiles along a red dashed line (Fig. 5C, third panel). Figure 5D shows that the intensity profiles were substantially influenced by the regional switching of the fluorescent solution. That is, in state *a*, intensity peak occurred in the left side of the cell nucleus and its value increased. In state *b*, intensity became uniform as its value increased. In state *c*, intensity peak occurred in the right side and decreased. Then, in state *d*, the intensity uniformly became 0.

To simplify the explanation of temporally varying intensity gradient, we separated the cell nucleus into zones L and R (Fig. 5C, first panel). Figure 5E shows that, in state *a*, the intensity (I_L) in zone L increased faster than that (I_R) in zone R. As depicted in the second left panel of the bottom of Fig. 5C, the fluorescent dye diffuses from fluorescent solution through zone L to zone R. Also, the diffusion path of zone L is shorter than that of zone R because of the ellipsoidal shape of the cell nucleus with *x*-directional length longer than *z*-directional length. These conditions make the increase rate of I_L higher than that of I_R, thereby increasing their intensity difference ($I_L - I_R$, Fig. 5F). In state *b*, $I_L - I_R$ decreased with the increasing I_L and I_R. The dye simultaneously diffused to both zones from the fluorescent solution along *z* direction, thereby decreasing the intensity difference. Then, in state *c*, I_L and I_R decreased. I_L decreases because photobleaching and dissociation of the dye occur in the cell nucleus, but the dye diffusion in zone L from the fluorescent solution is removed. I_R also decreases because the dye from the fluorescent solution substantially diffuses from zone R to zone L by the gradient of the dye concentration. We classify state *c* into states *c*1 and *c*2 based on the variation of I_L. In state *c*1, I_L rapidly decreased, and then, in state *c*2, I_L gradually decreased. This result implies that, in zone L in state *c*1, the photobleaching and dissociation of the dye are faster than the diffusion from zone R. Then, in state *c*2, those of the dye start to equilibrate with the diffusion from zone R. Because of the two-step change of I_L and nearly the constant decrease of I_R, $I_L - I_R$ decreases in state *c*1 and increases in state *c*2 (Fig. 5F). In state *d*, the fluorescent solution does not diffuse to both zones and photobleaching and dissociation of the dye continue, thereby making the intensity of the two zones almost 0. For comparison, we also measured the fluorescent intensity of a cell nucleus that locates in the left side of the target channel, and the intensities of zones L and R changed evenly (fig. S6).

Actuation of rods to play touchscreen piano

Last, we used a system consisting of one AA and five MAs (MA L1 to MA L5) connected in parallel (Fig. 6A and fig. S7) to actuate five rods

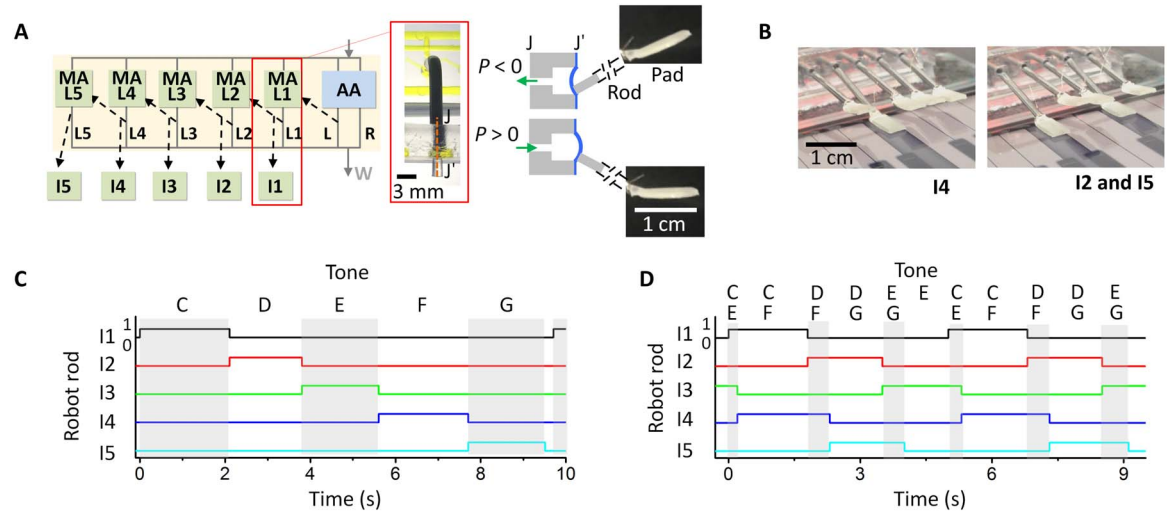

Fig. 6. Actuation of five rods for playing touchscreen piano. (**A**) Schematic of the device consisting of AA and five MAs (MA L1 to MA L5) for the actuation of five rods (I1 to I5). Section JJ′ shows the deflection of the membrane to actuate the rods. (**B**) Photographs of the rods playing the piano (photo credit: Zhenglin Li, Konkuk University). (**C** and **D**) Sequential and periodic rhythms generated by the interaction of the device and the piano. Each key is sequentially played in (C), and two keys are simultaneously played in (D).

(I1 to I5) to play a piano with a touchscreen. For the actuation of the rods, the pressure itself was necessary rather than solutions. Thus, we used only one solution to individually drive each MA. During the actuation of the rods, the solution moved from one input channel to one waste (W) output channel. The outlet of each MA was individually connected to the corresponding rod through an elastic membrane (Fig. 6A, inset). For example, owing to the positive output pressure of MA L1, the corresponding membrane inflated and rod I1 was tilted down to touch the corresponding key. Rod I1 was normally tilted up by the negative output pressure of MA L1. To maximize the change in its tilting angle, each rod was attached at the edge of the corresponding membrane. I1 to I5 were assigned to keys with tones C to G, respectively. Thus, the sequential periodic actuations were generated (Fig. 6B). When the period of the AA that triggers MA L1 was longer than the duration sum of the five MAs (9.7 s versus 9.5 s), keys were sequentially played one by one (Fig. 6C and movie S2). In comparison, when the period of the AA was shorter than the duration sum of five MAs (5 s versus 9.1 s), two keys were played in a simultaneous and periodic manner (Fig. 6D and movie S3).

DISCUSSION

On the basis of the analogy between microfluidic and electronic circuits, we have developed microfluidic devices that generate periodic sequential flows of multiple solutions without relying on any dynamic controllers. The devices converted the constant input of the water head pressure to the outputs of orchestrated, sophisticated flow and pressure pulses. As the functions of the devices were preset by the arrangements of AAs and MAs, users do not need to instruct the operation process to the devices through dynamic external controllers. Thus, user instructions and dynamic external controllers, which are the two typical requirements to generate sophisticated pulsed flow and are the bottlenecks for more widespread use of the devices, are truly eliminated.

In this study, the number of cases for available outflow in a target channel (T) is substantially larger compared to our previous work (*24*, *25*). This enables our current study to implement the sophisticated flow-timing control of multiple solutions without any dynamic controllers. With two input solutions, our previous work using AA has only three cases for flow timing control in T (fig. S8). In contrast, in Fig. 1B, the number is $2^{n+1}\,2^{m+1}-1$. Herein, the number of input solutions is $n + m + 2$, where n and m solutions are applied to the MAs on the right side and the left side of the AA, respectively, and two solutions are applied to the AA. For example, only with $n = 2$ and $m = 1$, the number of available cases is 31. With different connection combinations between AA and MAs, the system can generate complex periodic multiple parallel flows in a target channel (fig. S9). We note that, because each solution can have different fluidic parameters including chemical concentration, flow rate, and shear stress, the current approach allows us to implement highly sophisticated and various flow of multiple solutions. This is the feat that our previous work cannot achieve with its simple flow-timing control of two solutions.

Digital microfluidic circuits using Boolean operation can control the flow timing of multiple solutions (*16*–*18*). However, the circuits need encoded serial commands including three pulsatile inputs of clock, control, and trigger pressures. Because of the programmed dynamic inputs, the use of dynamic external controllers is inevitable for the operation of the circuits. In addition, for the circuit to convert the serial inputs to periodic multiple outputs, the circuit requires numerous serially cascaded microfluidic components and suffers significant pressure drop, thus limiting its scalability. In comparison, the operation process of our system is much simpler and has higher scalability. Furthermore, a fluidic timer circuit used a constant pneumatic pressure input and implemented six-step sequential flows (*27*), but it did not show sophisticated periodic flows that we presented with the orchestration of AA and MAs. Because of its requirement of comparatively high-pressure input, the timer circuit cannot be periodically triggered by the AA that we developed. The timer circuit operates in the pressure range of 30 to 60 kPa. However, the AA operates in ~10-kPa pressure so that it cannot trigger the timer circuits. This limits the capability for periodic and sophisticated control of flow timing for the timer circuit. As we have shown in Figs. 4 to 6, the various combinations of the AA and MA enables not only periodic flows but also sophisticated sequential flow

patterns. Besides, the pressure level of 30 to 60 kPa is hard to achieve with a water head in a laboratory environment typically having a room height of <3 m. Consequently, the timer circuit used an external controller for its static pressure source.

As a proof-of-principle demonstration, we have implemented the dynamic four-step staining of cell nuclei and the actuation of multiple rods to play the touchscreen piano. In the dynamic cell staining, we could not only regulate the sophisticated dynamic switching of fluorescent and blank solutions but also precisely control the interfacial position of the two solutions for the cell nucleus in each state. The interfacial position was maintained with less than 1-μm positional variation by the stable constant pressure of the water head input, thereby enabling dynamic cell staining with high stability. In comparison, even the externally driven microfluidic system with syringe pumps cannot achieve the dynamic cell staining with that high positional stability. For example, the positional variation caused by the pump is calculated to be ~22 μm because of the inherent flow rate fluctuations of the pump produced by the motion of the pump screw (*30*). The precise control of fluidic interface and dynamic flow switching in our study can be used in the studies of the spatial and temporal regulations of embryonic development (*14*), neuronal nematode behavior (*15*), biomolecular diffusion in cells (*10*, *11*), and cellular and bacterial chemotaxis (*12*, *13*).

As another example, the system consisting of an AA and multiple MAs actuated multiple rods to play a touchscreen piano, demonstrating its possible usability in soft robot applications. One of the challenges for untethered operation of soft robots is the development of autonomous actuators that enable the body to deliver preprogrammed behaviors. In a previous study, an AA was used to implement soft analogs of the control and power hardware and implemented 2-bit motion (*7*, *31*). For more sophisticated multigait and multijoint locomotion, however, the orchestration of sequential and periodic motion is indispensable. The smart arrangement of AAs and MAs demonstrated in this research enables more sophisticated and complex locomotion.

Currently, the size of our device is relatively larger than other microfluidic circuits (*16*–*19*). This is because the valves and membrane capacitors in our device are relatively large. However, scaling down the two components would be possible without significant change of device operational parameters including input pressure, flow-switching time, and flow rate. These parameters do not change if (i) mechanical capacitance of a membrane capacitor and (ii) opening threshold pressure of a valve are maintained. The mechanical capacitance of a membrane capacitor is $\propto w^6/t^3$ (*31*), where w and t are its width and thickness, respectively. In our device, w and t are 1.5 mm and 30 μm, respectively. If w decreases to 750 μm, then t needs to be decreased to 7.5 μm to maintain capacitance value. This thickness can be easily achieved by spin coating of polydimethylsiloxane (PDMS) in our device, thereby making it possible to maintain the capacitance value. If the width of a valve is decreased, then it increases the opening threshold pressure of the valve. However, the threshold pressure can be tuned by other valve elements including a seat, membrane, and surface of the valve. For example, we showed that the opening threshold pressure of a valve was reduced from 13 to 2 kPa by its valve-seat shape and surface coating (*32*). The threshold pressure is further decreased by reducing the thickness of the valve membrane. Hence, scaling down our device is feasible.

In terms of operation, our proposed platforms have an inherent limitation because, once the chips are fabricated, their operational ranges and functions are more limited than those that exploit external controllers. For instance, the flow rate and switching period are varied in a limited range unless the chip is redesigned, thus restricting versatility. However, when specific operational ranges and functions are determined in advance and the chips are designed accordingly, they will be useful like application-specific integrated circuit chips in electronics. Hence, we believe that the systems proposed in this study will be useful for numerous applications that need sequential periodic flow control without any user instructions and dynamic external controllers.

MATERIALS AND METHODS

Device fabrication

The devices were prepared with PDMS and were fabricated using multilayer soft lithography. We used SU-8 (models 2025 and 2075, MicroChem) to fabricate the top and bottom channels of a master mold. The thickness of the channels controlling fluidic resistances was 30 μm and that of the other channels was 100 μm. A 30-μm-thick middle layer for the elastic membrane was fabricated using PDMS spin coating on a glass plate and then placed in an oven at 120°C for 2 min. The master mold and glass plate were coated with trichloro(1H,1H,2H,2H-perfluorooctyl)silane (model 448931, Sigma-Aldrich) to allow PDMS to be easily peeled off after baking. The membrane connectors were punctured with a biopsy punch. The top and bottom chambers of the membrane capacitor were also punched with a biopsy punch without puncturing to ensure sufficient deflection of the membrane. Each layer was bonded after plasma treatment (model Cute-1MP, FemtoScience) and then placed in the oven at 120°C for 2 min. During the plasma treatment, we placed stamps on valve sheets and valve membranes to prevent bonding between them. We used 700-μm-wide stamps to cover valves with an 850-μm width for perfect closing of the valves. After the fabrication, we placed the device in a box filled with water, and the box was kept in a vacuum desiccator for 30 min to degas the device. The herringbone microfluidic mixer of the device shown in Fig. 4 had 60-μm-thick herringbone patterns. The membrane connector for the device shown in Fig. 6 was made of PDMS and was casted at 120°C for 30 min against a mold. The mold was fabricated using a three-dimensional (3D) printer (Form 2, Formlabs) using a transparent resin (FLPGCL 02, Formlabs). After mold fabrication, the mold was placed in the oven at 120°C for 2 hours to dry and cross-link the mold material. The membrane layer of the connector was spin-coated with a 200-μm thickness. The layers of the connector were bonded through plasma treatment. The pads of the rods were fabricated by the 3D printer. For the electrical contact between the pad and the piano with touchscreen, aluminum tape was applied on the pad bottom surface, and the tape was electrically connected to a power supply with 3 V using a 50-μm-diameter wire (44AWG) (fig. S7).

Reagents and cell

For the experiments represented in Figs. 3 and 4, we used a 2 mM blue (quinine hemisulfate salt monohydrate, Sigma-Aldrich) fluorescent dye in 5% sulfuric acid, 400 μM green (fluorescein sodium salt, Sigma-Aldrich) fluorescent dye in deionized water, and 400 μM red (rhodamine B, Sigma-Aldrich) fluorescent dye in 5% ethanol. For the experiment shown in Fig. 5, human umbilical vein endothelial cells (HUVECs) were cultured in T-flasks using standard cell culture methods. The cell seeding channel was coated with 0.4% (v/v) fibronectin in phosphate-buffered saline (PBS) at 37°C for 30 min. Then, the cell seeding channel was rinsed with PBS, and cell growth medium [Lonza, EGM-2 BulletKit (CC-3156 and CC4176)] was filled. Next, HUVECs were removed from the T-flask and injected into the cell seeding channel. For the attachment

of the cells on the channel surface, the device was placed in an incubator with 5% CO_2 at 37°C for 2 hours. To stain cell nuclei (Fig. 5), we used a 1 μM fluorescent dye (SYTO 85, Invitrogen) and tris-EDTA (TE) buffer.

Instruments

For flow visualization, we used a camera (model u-Nova20C, Novitec) on a microscope (model Ti-U, Nikon) to capture the red, green, and blue (RGB) images under different filters. In Fig. 4C (Fig. 4D), BF and RF (GF and RF) intensities were measured using DAPI (4′,6-diamidino-2-phenylindole) and TRITC (4′,6-diamidino-2-phenylindole and tetramethyl rhodamine isothiocyanate) [FITC (fluorescein isothiocyanate) and TRITC] filters, respectively, and collated. To characterize the fluorescent intensity of cell nuclei, a scientific Complementary Metal-Oxide-Semiconductor (sCMOS) camera (pco.edge 5.5, PCO) was used to capture the gray-scale image of the cell nuclei. Pressure sensors (PX309-015GI, Omega) and a pressure generator (AF1 Dual, Elveflow) were used to measure the pressure of the devices and the duration times of solution movement. The emission wavelength was measured by a fluorescence spectrophotometer (Cary Eclipse, Agilent).

Pressure conditions

The pressure conditions of the experiment shown in Fig. 3 were P_{Ai} = 10.5, P_i = 8.5, P_{Aref} = 0, P_{ref} = 9.5, and $P_o = P_{Ao}$ = −11 kPa. The common output flow rate of MAs was 195 μl min^{-1}. The pressure conditions of the experiment shown in Fig. 4 were $P_i = P_{Ai}$ = 9, P_{Aref} = 4.5, P_{ref} = 11.5 (left side), P_{ref} = 10.5 (right side), and $P_o = P_{Ao}$ = −11 kPa. A herringbone pattern microfluidic mixer had a flow rate of 28 μl min^{-1} with one valve open (states *a*, *c*, *e*, *f*, and *h*) and 48 μl min^{-1} with two valves open (states *b*, *d*, and *g*). The pressure conditions of the experiment shown in Fig. 5 were P_{Ai} = 9.5, P_{Aref} = 0, and P_{Ao} = −11 kPa; the input pressures of two valves and two MAs were P_i = 1.5 kPa and P_o = −3.5 kPa. The shear stress in the cell seeding channel was 27 dyne cm^{-2} at a flow rate of 135 μl min^{-1} with one valve open and 54 dyne cm^{-2} at a flow rate of 270 μl min^{-1} with two valves open. The pressure conditions of the experiment shown in Fig. 6 were $P_i = P_{Ai}$ = 9.7, P_{ref} = 11.4, and $P_o = P_{Ao}$ = −11 kPa. P_{Aref} = 3.1 kPa for 9.7-s duration of AA and P_{Aref} = 1.1 kPa for 5-s duration of AA.

SUPPLEMENTARY MATERIALS

Supplementary material for this article is available at http://advances.sciencemag.org/cgi/content/full/5/4/eaat3080/DC1

Open duration time of the valve of MA

Fig. S1. Working process of MA.

Fig. S2. Duration measurement and duration variation of MAs.

Fig. S3. Device for implementation of periodic stepwise variation of the concentration of a fluorescent solution.

Fig. S4. Device for implementation of the flow of three solutions that have different periods with overlapped intervals.

Fig. S5. Variation of fluorescent intensities by dilution and FRET.

Fig. S6. Device that periodically stains cell nuclei in four steps.

Fig. S7. Device used for actuating five rods to play touchscreen piano.

Fig. S8. Outflow combination by the connection between the target channel (T) and AA output channels.

Fig. S9. Periodic multiple parallel flows.

Movie S1 (.mp4 format). Dynamic staining of cell nuclei.

Movie S2 (.avi format). Playing a touchscreen piano with the touch of keys one by one.

Movie S3 (.avi format). Playing a touchscreen piano with the touch of two keys simultaneously.

REFERENCES AND NOTES

1. J. J. Richardson, J. Cui, M. Björnmalm, J. A. Braunger, H. Ejima, F. Caruso, Innovation in layer-by-layer assembly. *Chem. Rev.* **116**, 14828–14867 (2016).
2. E. Ahn, T. Lee, M. Gu, M. Park, S. H. Min, B.-S. Kim, Layer-by-layer assembly for graphene-based multilayer nanocomposites: The field manual. *Chem. Mater.* **29**, 69–79 (2017).
3. W.-B. Du, Q. Fang, Z.-L. Fang, Microfluidic sequential injection analysis in a short capillary. *Anal. Chem.* **78**, 6404–6410 (2006).
4. P. B. Allen, A. D. Ellington, Sequential injection analysis for optimization of molecular biology reactions. *Anal. Chem.* **83**, 2194–2200 (2011).
5. D. Rus, M. T. Tolley, Design, fabrication and control of soft robots. *Nature* **521**, 467–475 (2015).
6. R. F. Shepherd, F. Ilievski, W. Choi, S. A. Morin, A. A. Stokes, A. D. Mazzeo, X. Chen, M. Wang, G. M. Whitesides, Multigait soft robot. *Proc. Natl. Acad. Sci. U.S.A.* **108**, 20400–20403 (2011).
7. M. Wehner, R. L. Truby, D. J. Fitzgerald, B. Mosadegh, G. M. Whitesides, J. A. Lewis, R. J. Wood, An integrated design and fabrication strategy for entirely soft, autonomous robots. *Nature* **536**, 451–455 (2016).
8. A. Goldbeter, Biological rhythms: Clocks for all times. *Curr. Biol.* **18**, R751–R753 (2008).
9. A. Yan, G. Xu, Z.-B. Yang, Calcium participates in feedback regulation of the oscillating ROP1 Rho GTPase in pollen tubes. *Proc. Natl. Acad. Sci. U.S.A.* **106**, 22002–22007 (2009).
10. J. C. Politz, E. S. Browne, D. E. Wolf, T. Pederson, Intranuclear diffusion and hybridization state of oligonucleotides measured by fluorescence correlation spectroscopy in living cells. *Proc. Natl. Acad. Sci. U.S.A.* **95**, 6043–6048 (1998).
11. S. Papadopoulos, V. Endeward, B. Revesz-Walker, K. D. Jürgens, G. Gros, Radial and longitudinal diffusion of myoglobin in single living heart and skeletal muscle cells. *Proc. Natl. Acad. Sci. U.S.A.* **98**, 5904–5909 (2001).
12. N. L. Jeon, H. Baskaran, S. K. W. Dertinger, G. M. Whitesides, L. Van De Water, M. Toner, Neutrophil chemotaxis in linear and complex gradients of interleukin-8 formed in a microfabricated device. *Nat. Biotechnol.* **20**, 826–830 (2002).
13. Z. Li, Q. Cai, X. Zhang, G. Si, Q. Ouyang, C. Luo, Y. Tu, Barrier crossing in *Escherichia coli* chemotaxis. *Phys. Rev. Lett.* **118**, 098101 (2017).
14. E. M. Lucchetta, J. H. Lee, L. A. Fu, N. H. Patel, R. F. Ismagilov, Dynamics of *Drosophilia* embryonic patterning network perturbed in space and time using microfluidics. *Nature* **434**, 1134–1138 (2005).
15. N. Chronis, M. Zimmer, C. I. Bargmann, Microfluidics for in vivo imaging of neuronal and behavioral activity in *Caenorhabditis elegans*. *Nat. Methods* **4**, 727–731 (2007).
16. M. Rhee, M. A. Burns, Microfluidic pneumatic logic circuits and digital pneumatic microprocessors for integrated microfluidic systems. *Lab Chip* **9**, 3131–3143 (2009).
17. N. S. G. K. Devaraju, M. A. Unger, Pressure driven digital logic in PDMS based microfluidic devices fabricated by multilayer soft lithography. *Lab Chip* **12**, 4809–4815 (2012).
18. J. A. Weaver, J. Melin, D. Stark, S. R. Quake, M. A. Horowitz, Static control logic for microfluidic devices using pressure-gain valves. *Nat. Phys.* **6**, 218–223 (2010).
19. W. H. Grover, R. H. C. Ivester, E. C. Jensen, R. A. Mathies, Development and multiplexed control of latching pneumatic valves using microfluidic logical structures. *Lab Chip* **6**, 623–631 (2006).
20. T. V. Nguyen, P. N. Duncan, S. Ahrar, E. E. Hui, Semi-autonomous liquid handling via on-chip pneumatic digital logic. *Lab Chip* **12**, 3991–3994 (2012).
21. P. N. Duncan, T. V. Nguyen, E. E. Hui, Pneumatic oscillator circuits for timing and control of integrated microfluidics. *Proc. Natl. Acad. Sci. U.S.A.* **110**, 18104–18109 (2013).
22. T. Thorsen, S. J. Maerkl, S. R. Quake, Microfluidic Large-Scale Integration. *Science* **298**, 580–584 (2002).
23. Q. Zhang, M. Zhang, L. Djeghlaf, J. Bataille, J. Gamby, A.-M. Haghiri-Gosnet, A. Pallandre, Logic digital fluidic in miniaturized functional devices: Perspective to the next generation of microfluidic lab-on-chips. *Electrophoresis* **38**, 953–976 (2017).
24. S.-J. Kim, R. Yokokawa, S. C. Lesher-Perez, S. Takayama, Multiple independent autonomous hydraulic oscillators driven by a common gravity head. *Nat. Commun.* **6**, 7301 (2015).
25. V. B. Dang, S.-J. Kim, Water-head-driven microfluidic oscillators for autonomous control of periodic flows and generation of aqueous two-phase system droplets. *Lab Chip* **17**, 286–292 (2017).
26. Z. Li, S.-J. Kim, Pulsatile micromixing using water-head-driven microfluidic oscillators. *Chem. Eng. J.* **313**, 1364–1369 (2017).
27. J. Kang, D. Lee, Y. J. Heo, W. K. Chung, Fully chip-embedded automation of a multi-step lab-on-a-chip process using a modularized timer circuit. *Lab Chip* **17**, 3891–3897 (2017).
28. A. D. Stroock, S. K. W. Dertinger, A. Ajdari, I. Mezić, H. A. Stone, G. M. Whitesides, Chaotic mixer for microchannels. *Science* **295**, 647–651 (2002).
29. G. W. Gordon, G. Berry, X. H. Liang, B. Levine, B. Herman, Quantitative fluorescence resonance energy transfer measurements using fluorescence microscopy. *Biophys. J.* **74**, 2702–2713 (1998).
30. C. Kim, D. H. Hwang, S. Lee, S.-J. Kim, Water-head pumps provide precise and fast microfluidic pumping and switching versus syringe pumps. *Microfluid. Nanofluidics* **20**, 4 (2016).
31. B. Mosadegh, C.-H. Kuo, Y.-C. Tung, Y.-s. Torisawa, T. Bersano-Begey, H. Tavana, S. Takayama, Integrated elastomeric components for autonomous regulation of sequential and oscillatory flow switching in microfluidic devices. *Nat. Phys.* **6**, 433–437 (2010).

32. J. Shin, H. Park, V. B. Dang, C.-W. Kim, S.-J. Kim, Elastomeric microfluidic valve with low, constant opening threshold pressure. *RSC Adv.* **5**, 23239–23245 (2015).

Acknowledgments

Funding: This work was supported by the National Research Foundation of Korea (NRF) grant funded by the Korea government (MSIP) (NRF-2016R1A5A1010148, 2017R1A2B4005955), the Korea Institute of Energy Technology Evaluation and Planning (KETEP), and the Ministry of Trade, Industry and Energy (MOTIE, 20174010201490). **Author contributions:** Z.L. designed and fabricated devices, as well as performed the device experiments. S.-J.K. conceived, supervised, and guided the work. Z.L. and S.-J.K. wrote the manuscript. **Competing interests:** The authors declare that they have no competing interests. **Data and materials availability:** All data needed to evaluate the conclusions in the paper are present in the paper and/or the Supplementary Materials. Additional data related to this paper may be requested from the authors.

Submitted 19 February 2018
Accepted 1 March 2019
Published 19 April 2019
10.1126/sciadv.aat3080

Citation: Z. Li, S.-J. Kim, Autonomous microfluidic actuators for periodic sequential flow generation. *Sci. Adv.* **5**, eaat3080 (2019).

Autonomous microfluidic actuators for periodic sequential flow generation

Zhenglin Li and Sung-Jin Kim

Sci Adv **5** (4), eaat3080.
DOI: 10.1126/sciadv.aat3080